TÜBİTAK

Turkish Journal of Earth Sciences

http://journals.tubitak.gov.tr/earth/

Research Article

Turkish J Earth Sci
(2023) 32: 652-665

doi:10.55730/1300-0985.1866

A controlled source tomography in Sarımeşe, İzmit, at the western section of North Anatolian Fault Zone

Tuğçe ERGÜN

Regional Earthquake and Tsunami Monitoring Center, Kandilli Observatory and Earthquake Research Institute, Boğaziçi University, İstanbul, Turkey

Received: 22.07.2022 • **Accepted/Published Online:** 08.06.2023 • **Final Version:** 28.07.2023

Abstract: A high-resolution two-dimensional tomographic velocity image in the eastern Marmara region along a 1.2 km long N-S trending seismic profile, which crosses the surface rupture of the İzmit earthquake on the North Anatolian Fault (NAF) is presented. A vibroseis source at more than 180 points with 50 receivers was used along the long profile. A regularized inversion technique was applied to the first arrival travel times. More than 6500 first arrivals from 129 shot gathers were analyzed to construct velocity images and were qualitatively evaluated for the fault zone-related effects. The velocity model was constrained to a maximum depth of 175 m. The results indicate a fault zone of ~100 m thick with clear velocity contrasts with surrounding blocks. The P wave velocity on the southern block varies between a range of 1.4–1.7 km/s and 1.7–2.0 km/s on the northern block the velocity decreases to 1.4 km/s within the fault zone down to 100–150 m depth. Three component recordings and fan shots also indicate the presence of the fault zone consistent with the tomographic image.

Keywords: North Anatolian Fault, controlled source tomography, fault zone imaging

1. Introduction

The fault zones (FZ) are narrow, heterogeneous, fracture zones embedded between relatively persistent materials (Ben-Zion, 1998). Determining the physical properties of a FZ is fundamental for developing a realistic model of the earthquake process. The zones may have thicknesses of several tens of meters to several hundreds of meters at the surface (Li et al., 2000) and are relatively narrower at depth. They are associated with lower seismic velocities than the surrounding rocks and form low-velocity channels which may trap seismic energy and display specific wave propagation effects such as head waves, anisotropy, scattering, and attenuation. Several observational studies have provided evidence of these fault zone related effects. Detailed descriptions and properties of the fault zone waves are presented by Cormier and Spudich (1984), Ben-Zion and Aki (1990), Ben-Zion (1998), Rovelli et al. (2002), Peng et al. (2003), McGuire and Ben-Zion (2005), and Malin P.E. (2020). Leary et al. (1987), Igel et al. (1997, 2002), Jahnke et al. (2002), and Fohrmann et al. (2001, 2004) have discussed properties of guided waves in irregular 2-D and 3-D FZ structures.

The North Anatolian Fault Zone (NAFZ) is the northern boundary of the westward-moving Anatolian block and connects the compressional regime in eastern Anatolia with the extensional regime in the Aegean Sea region (McKenzie, 1972; Şengör, 1979; Barka, 1992). NAF which has been interpreted as a transform fault originating from the late Miocene collision of the Arabian and Eurasian plates (McKenzie, 1972), extends from the Karlıova to the Mudurnu Valley on a single strand splays into branches in the Marmara and North Aegean regions (Barka and Kadinsky-Cade 1988; Barka, 1992). The NAF which accommodates most of the westward motion of Turkey has a narrow and localized character and is clearly defined by the strike-slip surface along its entire length. The fault is associated with a series of major earthquakes since 1939 and the most recent one is the 17 August 1999 İzmit earthquake (Mw = 7.4) which ruptured a 150 km long segment of the fault. The earthquake was a right-lateral strike-slip with maximum offsets reaching 4 to 5 m (Barka et al., 2002). Intense aftershock activity followed the main shock and a M_w = 7.2 magnitude earthquake occurred in Düzce three months later (Karabulut et al., 2002; Özalaybey et al., 2002; Aktar et al., 2004). Several studies related to the fault zone following the earthquake were undertaken in the region. A tomographic image crossing the NAF in the eastern Marmara region revealed

* Correspondence: afacan@boun.edu.tr

low-velocity fault zone correlated with the seismicity (Karabulut et al., 2003). Ben-Zion et al. (2003) analyzed a large seismic data set recorded 6 months after the 1999 Mw = 7.4 İzmit earthquake by a local network on the Karadere-Düzce branch of the North Anatolian Fault (NAF). They observed large amplifications at sites within tens of m from the surface expression of the rupture. The analysis showed that the depth extent of the structure in the fault zone producing trapped waves is 3–4 km. Shear wave splitting measurements on the Karadere-Düzce branch of NAF by Peng and Ben-Zion (2004) show anisotropy confined to the upper 3–4 km. Peng and Ben-Zion (2006) analyzed temporal variations of seismic velocity along this segment of the NAF using seismograms generated by repeating earthquake clusters in the aftershock zones of the İzmit and Düzce earthquakes. They observed clear step-like delays in the direct S and early S-coda waves (sharp seismic velocity reduction) immediately after the Düzce main shock followed by gradual logarithmic-type recoveries. Zor et al. (2010) presented the shear wave velocity structure of the İzmit Gulf area from the surface wave and single-station microtremor methods. The results indicate that the sediment–bedrock depth reaches about 1200 m in the deepest part of the İzmit basin. Özalaybey et al. (2011) also investigated the 3-D basin structure in the İzmit Gulf area by single-station microtremor and gravity methods indicating that the maximum basin depth is 1.4 km for the İzmit basin. The northern part of İzmit Gulf essentially consists of young shallow sediments, beneath these lie a Triassic and Paleozoic sandstone, clay stone, and marn. The southern zone corresponds to an olistolitic complex, which is composed of Eosen volcanics (schist, serpentinite, and andesite) (Doğan, B., 1998). Lower Paleozoic – Upper Cretaceous aged metamorphic rocks lie in the basement. These geologic units are composed of two levels. First level is represented by metaclactics such as clorite, serizite, calc, talc and mica schists, and the latter is represented by recrystallized limestone and low grade meta carbonates (Doğan, B., 1998). The youngest units of the area are alluvium and talus. Sarımeşe pull – apart basin is formed as a result of long-term faulting in between the Pliocene and Quaternary periods. The area between İzmit Gulf and Sapanca Lake consists of Middle Pleistocene and Holocene sediments overlain by uncorformable a pre-Neogene basement. Between 30 to40 m thick sediments accumulated over the widespread 30–35 km thick bog material. This sediment settlement and the morphologic structure of the area are controlled by the Northern Branch of the North Anatolian Fault Zone (Aksoy, M.E., 2002; Yiğitbaş et al., 2004).

The detailed analysis of fault zones plays an important role in problems related to fault mechanics, dynamic rupture, wave propagation, and seismic hazard. In this manner, during the fall of 2003, seismic refraction data were collected in the eastern Marmara Region on the North Anatolian Fault Zone (NAFZ) near İzmit along a 1.2 km profile. The area is located between İzmit Bay and Sapanca Lake (Figure 1). The fault, ruptured during the 17 August 1999 earthquake, was clearly exposed on the surface where the thickness of the sediments in the basin is expected to be greater than several hundred m. Figure 2 shows the seismic array deployed along and across the ruptured segment of the NAFZ during the İzmit earthquake. The array is located in the İzmit basin, 5 km west of the epicenter of the İzmit earthquake. The coseismic slip observed on the surface was between 1–3 m in the basin. The traces of the surface rupture could still be recognized on the surface four years after the earthquake. The thickness of the fault zone on the surface appeared to be varying from several meters to several hundred meters. The basin is approximately 20 km wide and 50 km long with metamorphic basement overlain by quaternary sediments. The thickness of the sediments is estimated at between 0.6–1.4 km (Özalaybey et al., 2011).

The primary objective of this study is to determine the shallow velocity structure on the North Anatolian Fault in Sarımeşe near İzmit rupture zone via 2-D tomography inversion. Determination of a reliable tomographic image, estimating the thickness of the fault zone and defining the travel time anomalies will shed a light on the behavior of fault over time and seismic hazard.

2. Data acquisition and processing

The data were acquired along a 1.2 km long N-S profile which has been attentively chosen in order to cross the fault (Figure 2). A mild topography exists along the profile and the elevation difference between north and south is approximately 12 m increasing from south to north. The profile was cut by a 10 m wide irrigation channel. The fault trace on the surface is located on the north of the channel. A total of 45 Reftek- 125 and 5 Reftek-130 recorders were equipped with 4Hz and 12Hz vertical components and 3-component geophones respectively. The shot spacing was 5 m for inline, 200 m for fan shots and the receiver spacing was varying from 10 m to 20 m. More than 180 inline, 10 fan shots were fired using a vibroseis source (Figure 2). Due to the vegetation, the geometry of the line was not straight but crocked on the south of the fault zone. The data were recorded continuously with a 100 Hz sampling rate. Both computed and recorded sweep signals were tested to obtain conventional shot gathers and concluded that the computed sweep signal provides a better source wavelet. Figure 3 shows the uncorrelated shot gather and correlated shot gather using theoretical vibroseis sweep signal. Uncorrelated shot gather shows that the S/N ratio decreases fast at distances greater than

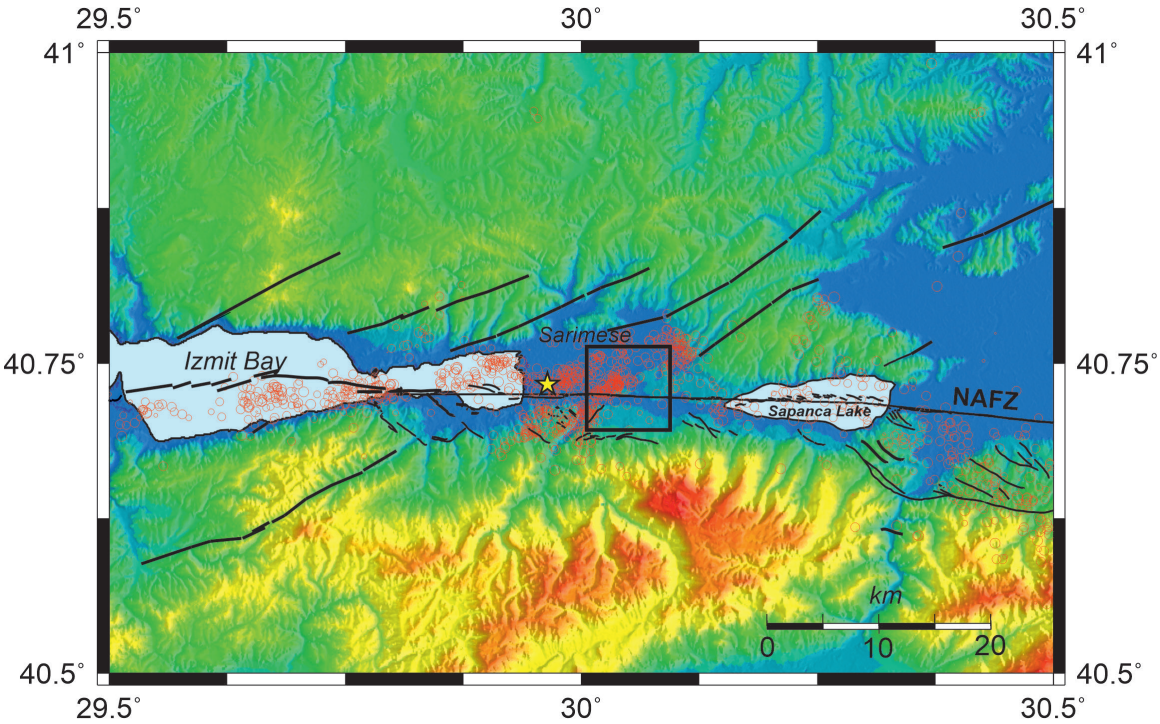

Figure 1. Location map of the study area (black square). Yellow star indicates the location, red circles refer to the aftershock activity (Karabulut et al., 2002) of the 17 August 1999 İzmit earthquake. Black lines show the active faults (Emre et. al., 2013).

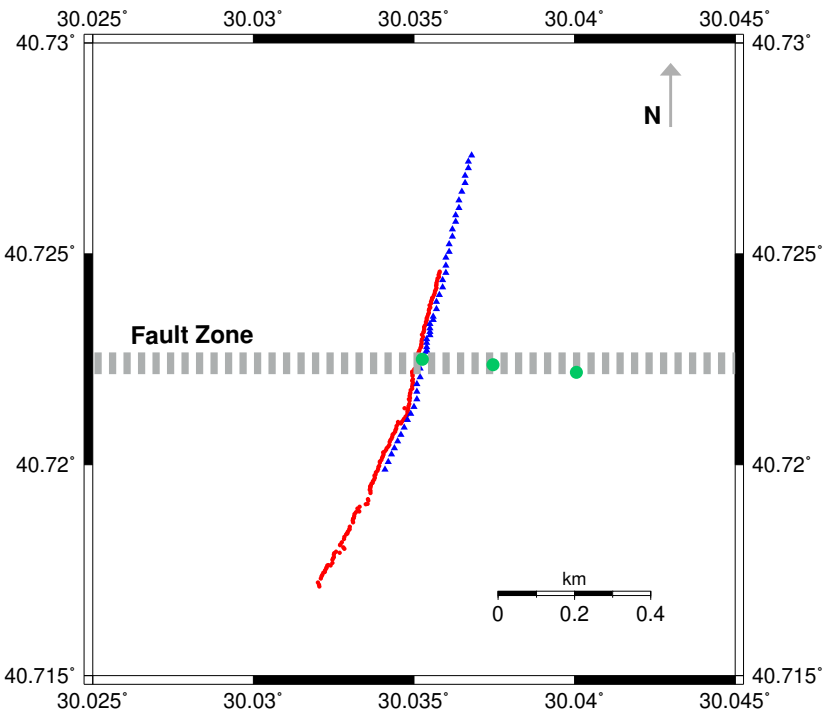

Figure 2. The source-receiver geometry of the experiment. Blue triangles indicate the receiver locations and red circles indicate shot locations. Green circles are the fan shots.

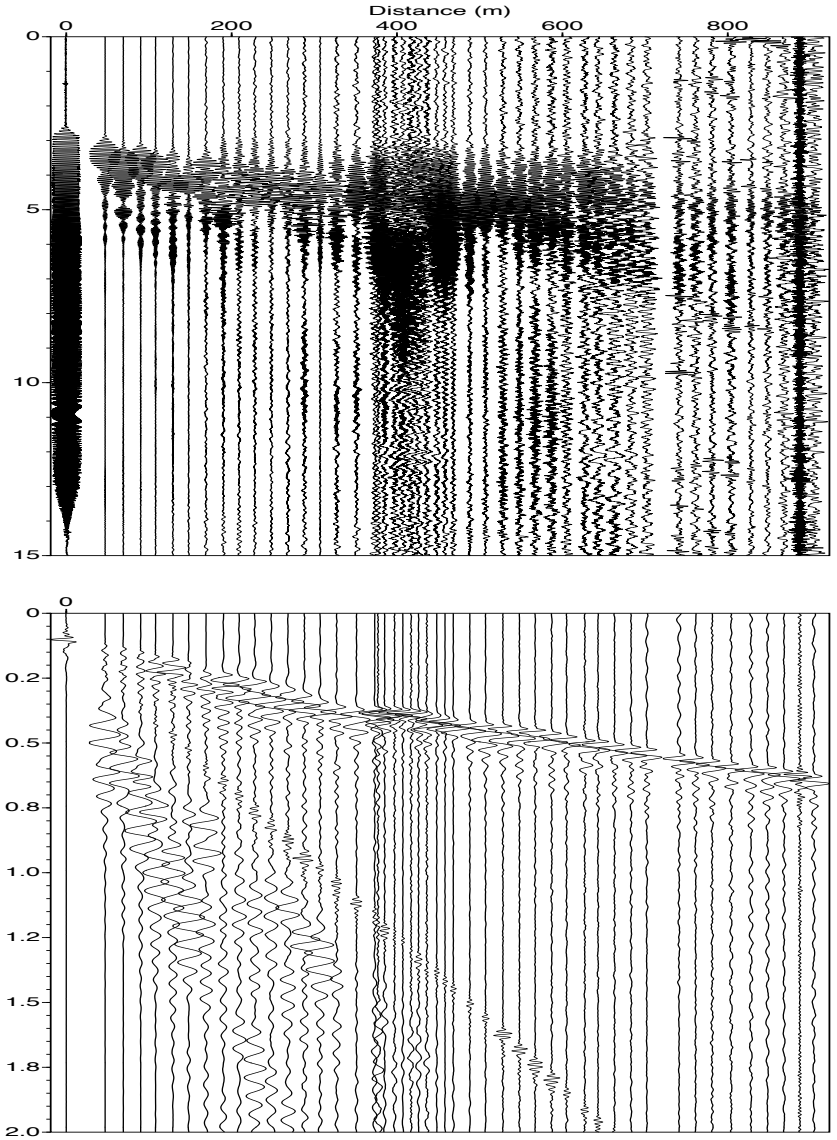

Figure 3. Uncorrelated shot gather (top) and correlated shot gather using theoretical vibroseis sweep signal (bottom).

400 m. The trace at 0 m shows the sweep signal recorded next to the vibrator truck.

One hundred and twenty-six shot gathers were selected and more than 5000 first arrivals were picked. The uncertainty for each pick was assumed as 10 ms and constant for each shot gather. One-third of the shot gathers were ignored due to the low-signal noise ratio or large uncertainty on the origin times. Figure 4 displays the first arrival times of the selected shot gathers along the profile. The coverage in the center of the profile is not uniform due to the lack of shot and receiver points within the irrigation channel. Travel time curves show strong velocity variations along the profile. This is more pronounced in the middle of the profile, between 550 and 700 m, where the fault scarps on the surface are clearly observable. The elevation correction was applied by introducing a shallow layer with a very low velocity (100 m/s). The sources and receivers were put on the basement of the shallow layer and the velocity of the surface layer was fixed during the inversion.

3. Method

The inversion technique used in this study is developed by Vidale (1988) and modified by Hole and Zelt (1995). The method is using a regularized inversion scheme with flattest and smoothest perturbation constraints. The models are parameterized using uniform square grids. The forward grid has much smaller grid spacing than the

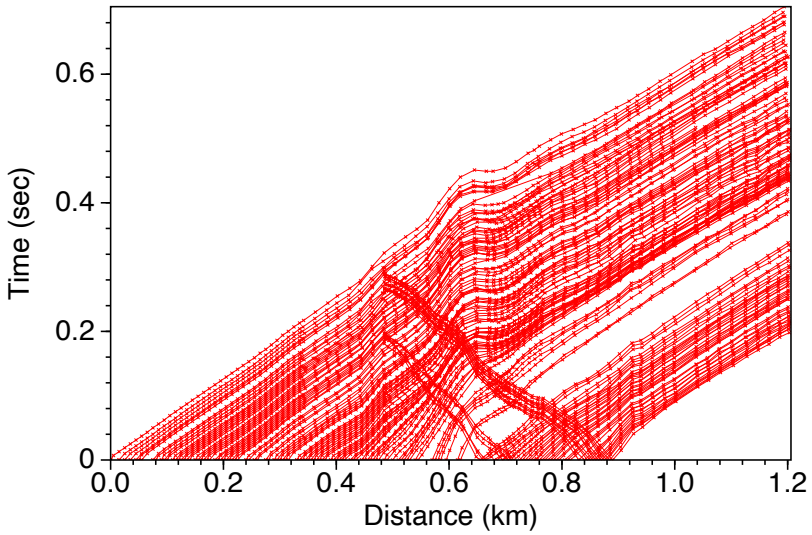

Figure 4. The selected travel time distance curves.

inverse grid since the accuracy of the computed travel times using Eikonal equation depends on the grid spacing, which requires finer gridding. On the other hand, the inverse grid with the smoothness constraints should be larger to keep the linear system overdetermined.

One of the main difficulties encountered in tomographic studies is the determination of the reliability of the results. Tomographic images reflect not only true velocity heterogeneities but also the effect of data errors, model parameterization, and ray path geometry. The correct assessment of model parameterization in seismic tomography is a difficult task since the resolution of the solution is highly affected by the chosen model parameters. Synthetic tests such as checkerboard test provide information relevant to the model parameterization, damping factor and solution quality (Humpreys and Clayton, 1988; Zelt, 1988). Checkerboard test was performed using the source-receiver configuration of the experiment to check the resolvability of the final model with different model parameters. Initial velocity model was constructed by assuming a velocity gradient on the background and cells with 5 × 5 m in size perturbed ±0.6 km/s alternately (Figure 5). The upper 100 m and the central part of the pattern appear quite well retrieved due to the complete ray path coverage, whereas at edge of the model the effects generated by the lack of crossing rays are evident.

One-dimensional velocity model was constructed from the best fit to the average of the observed travel time. The velocity model contains several layers of increasing velocity with depth. The velocities are starting at 1.4 km/s at the surface and increasing to 2.2 km/s at a depth of 260 m. Strong velocity contrast from the shot gathers indicating any shallow reflector was not observed. The high apparent velocities observed between 550 and 700 m are the results of the lateral velocity variations. Also three velocity models (blue, red, and green lines in Figure 6) constructed to test whether there is any dependency of the inversion on the initial model (Figure 6).

The velocity model was defined on a uniform 1 × 1 m grids extending from 0 to 1.2 km in x-direction and 0 to 0.2 km in z-direction for forward calculations. A grid size of 10 m in lateral and vertical directions was used during the inversion. The parameterization requires 1200 velocity points to be determined from the inversion.

The inversion is based on minimization of data misfit and model roughness to provide the

smoothest model appropriate for the data. To assess the quality of the inversion, travel time RMS residuals and normalized data misfit ($\chi 2$) parameters are controlled in every iteration. Optimum values of the free parameters in the inversion, which controls horizontal smoothness and model roughness, were used in order to produce a minimum structure model. Three different initial velocity models were used in tomography to see how the final velocity model is dependent to the initial model. Figure 7 shows the travel time errors as a function of distance for the initial and final models. The RMS residuals for the initial and the final models were 40ms and 5ms respectively. The largest travel time errors observed using the initial velocity model at distances between 500 and 800 m is due to the lateral variations in the velocity model. The final velocity model reduced the errors which shows more uniform distribution along the profile.

4. Results

Figure 8 displays the results of the tomographic inversion and ray coverage for the final P-wave velocity model.

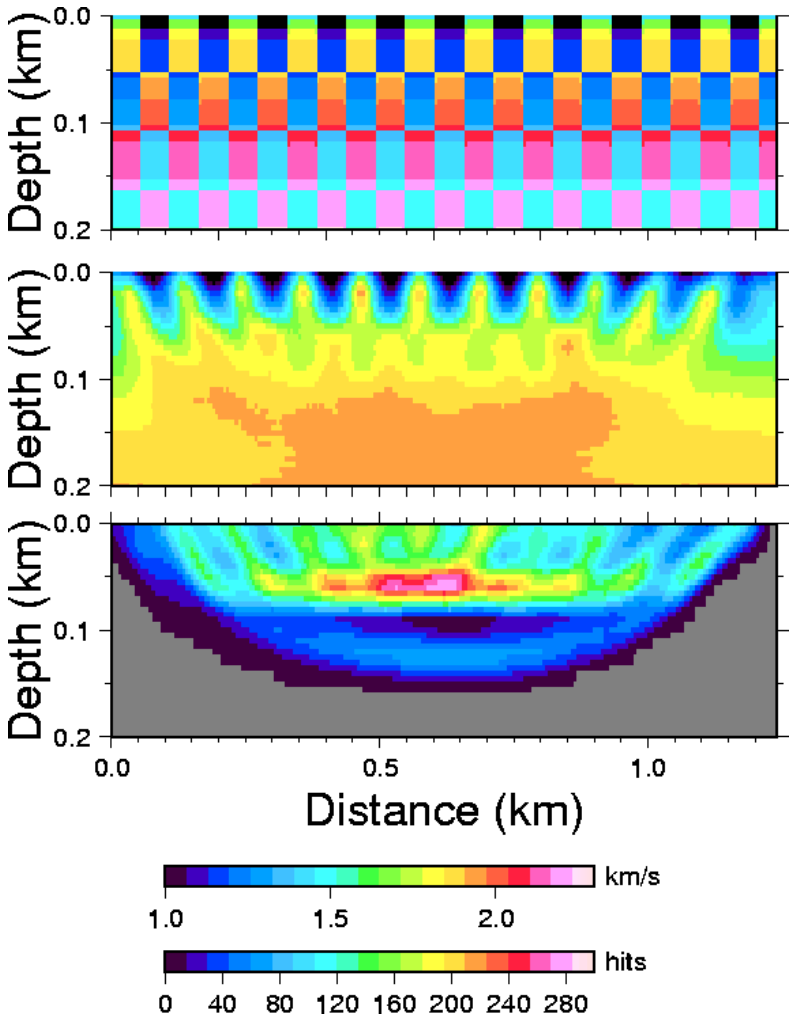

Figure 5. Results of the checkerboard tests, upper figure is the perturbed initial velocity model, middle shows the final P-wave velocity model derived from the inversion with smoothness/flatness regularization constraint s mwz = 0.5, lower figure is the ray hitcount.

Dependency on the initial models is not significant when the ray hitcount is large therefore the velocity structure is well resolved. A robust and high resolution travel time image requires dense ray sampling and rays crossing at variety of angles. The ray coverage indicates that the final velocity model is well constrained down to 175 m depth. Similar results were obtained from alternate initial models and different inversion parameters with an exception at shallower depths. According to Zor et al. (2010) and Özalaybey et al. (2011) the sediment–bedrock depth reaches about 1.4 km in the deepest part of the İzmit basin, therefore the basement is not expected to be seen from the travel time tomography. The seismic profile crosses the fault between 600–700 m. The irrigation channel with a width of approximately 10 m appears between 550 and 600m. P-wave velocity of the sediments on the southern part of the channel increases from 1.4 km/s at the surface to 1.7 km/s at the depth of 150 m. Relatively high velocities exist on the northern part of the profile varying from 1.7 km/s at the surface to 2.0 km/s at the depth of 200 m. The lowest velocities, 0.7–0.8 km/s are observed between 550 and 600 m where the irrigation channel is located. On the continuation of the irrigation channel between 650 and 750 m the velocities are approximately 0.2 km/s lower than the average velocities on the northern block. Highest velocities (2.0–2.2 km/s) are observed in a localized zone starting at a depth of 80m and continuing to the bottom of the model. This zone is located below the lowest velocity region and appears to have a limited extent in the horizontal direction.

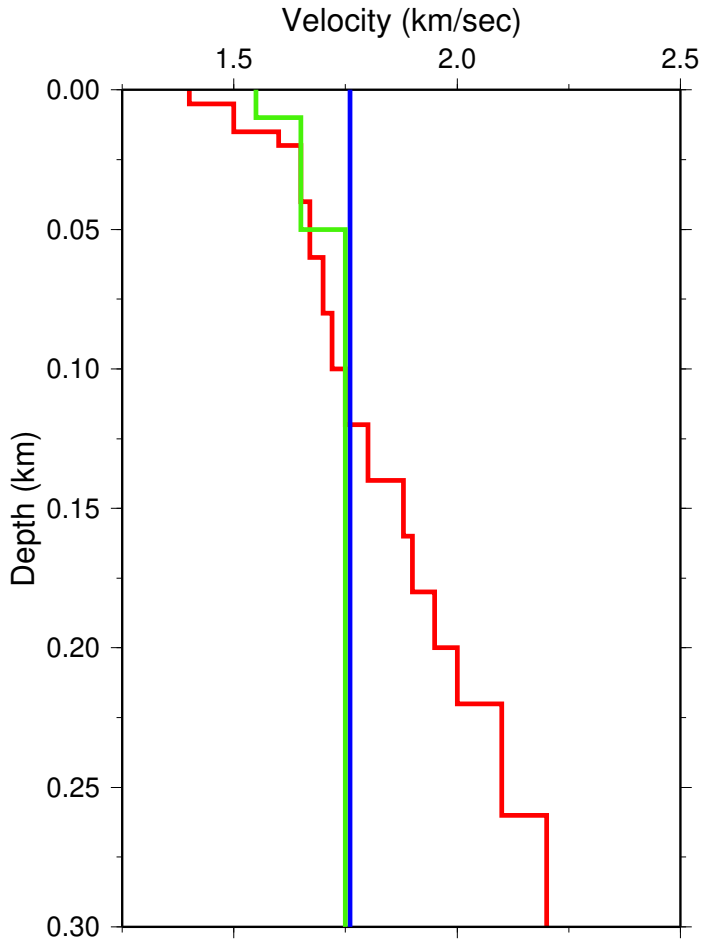

Figure 6. Three initial different velocity models for tomography (blue, green, and red one). Red line indicates the preferred average 1-D velocity model obtained from the travel time observations, green line includes three layers and the blue one represents a constant velocity model.

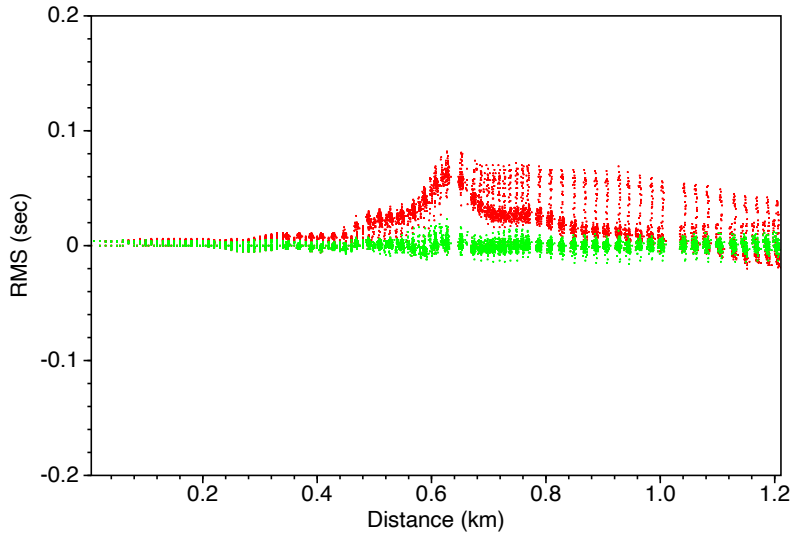

Figure 7. Travel time residuals computed from the preferred starting model (red) and final model (green) after inversion.

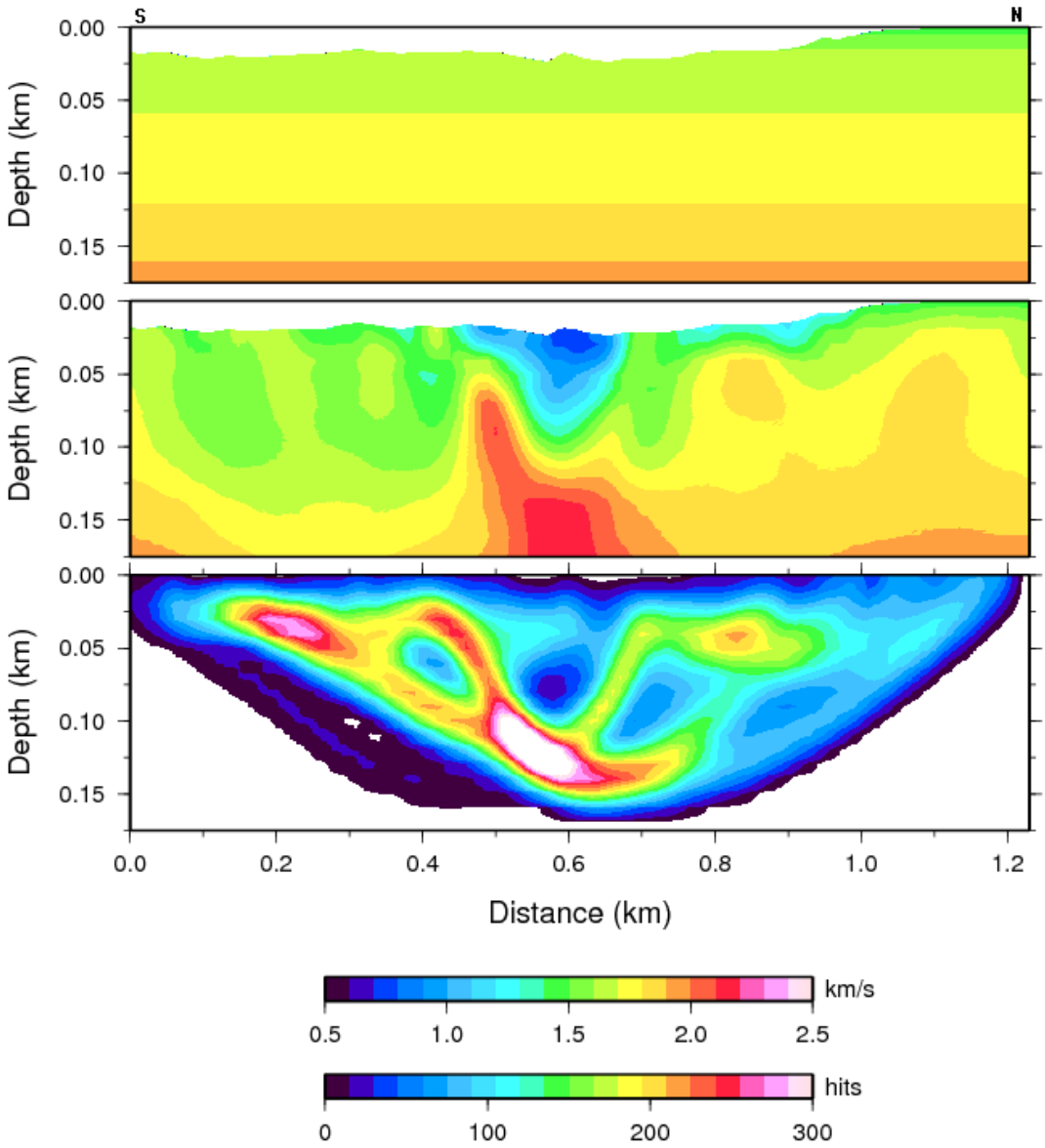

Figure 8. Upper: Initial P-wave velocity model; middle: P-wave velocity model obtained from tomographic inversion; lower: ray cell hitcount.

Figures 9, 10, and 11 show the final tomographic image and fan shots at distances of 0 m, 200 m, and 400 m respectively. The high amplitude surface waves are observed at receivers near the fault zone. Since the amplitudes of the surface waves are rapidly decreasing for receivers away from the fault zone, the observed wavefield indicates trapped waves generated along the fault zone. The separation of the surface waves and trapped waves from the body waves are apparent for the shots at greater distances (compare 0 m and 400 m fan shots in Figure 9 and 11). It is also important to realize that there is significant asymmetry of the wavefield on both sides of the fault zone. The arrival times on the northern part of the fault zone reveal interesting character. There is a large travel time jump at a distance of 900 m. If the high-velocity anomaly is not local but has larger spatial dimensions or has continuity along the fault zone it would create asymmetries and travel time anomalies on the first arrivals as well as diffraction patterns on the wavefield. Such asymmetries are created, e.g., by head waves propagating along vertical discontinuities with higher velocities.

Figure 12 shows the final tomographic image and two shot gathers at two sides of the fault zone. The first shot gather

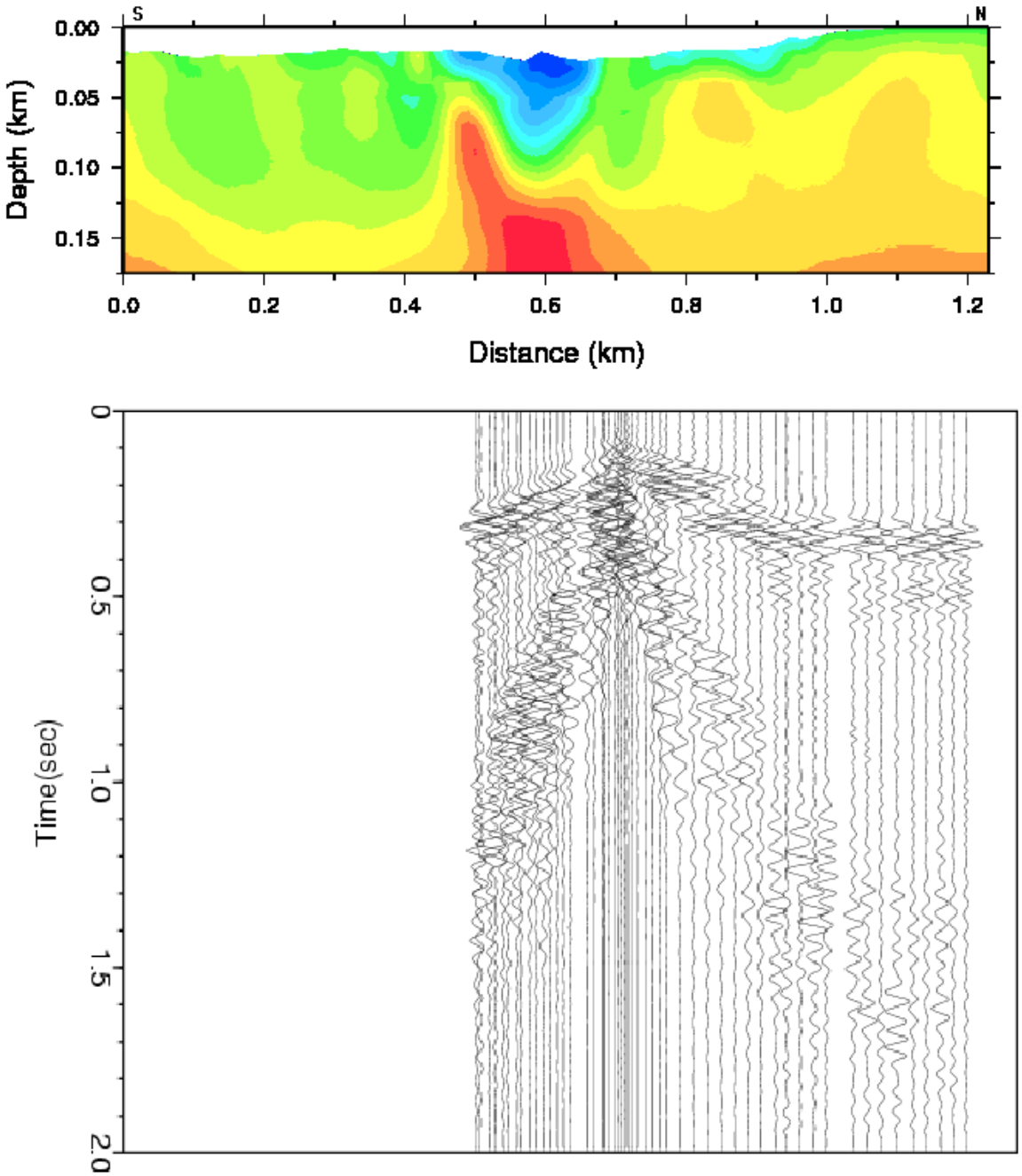

Figure 9. The final tomographic image and fan shot at adistance of 0 m. FZ: Fault Zone, IC: Irrigation Channel.

presented in the figure has a clear diffraction pattern with the apex at a distance of approximately 500 m. This is an independent confirmation of the high-velocity anomaly observed on the tomographic image. On the other hand, the second shot gather displayed in Figure 12, contains fault zone trapped waves between distances of 650 and 750 m. Fault zone trapped waves are clearly separated from surface waves with large amplitudes.

5. Discussion and conclusions

The tomographic velocity model clearly reflects the velocities at shallow depths (<20m) that are not well constrained due to the lack of near offset data, therefore these velocities are sensitive to the initial model. The ray coverage is not homogeneous, greater and deeper ray coverage is observed in the middle of the profile. The obtained velocity model is constrained to a maximum depth of 175 m.

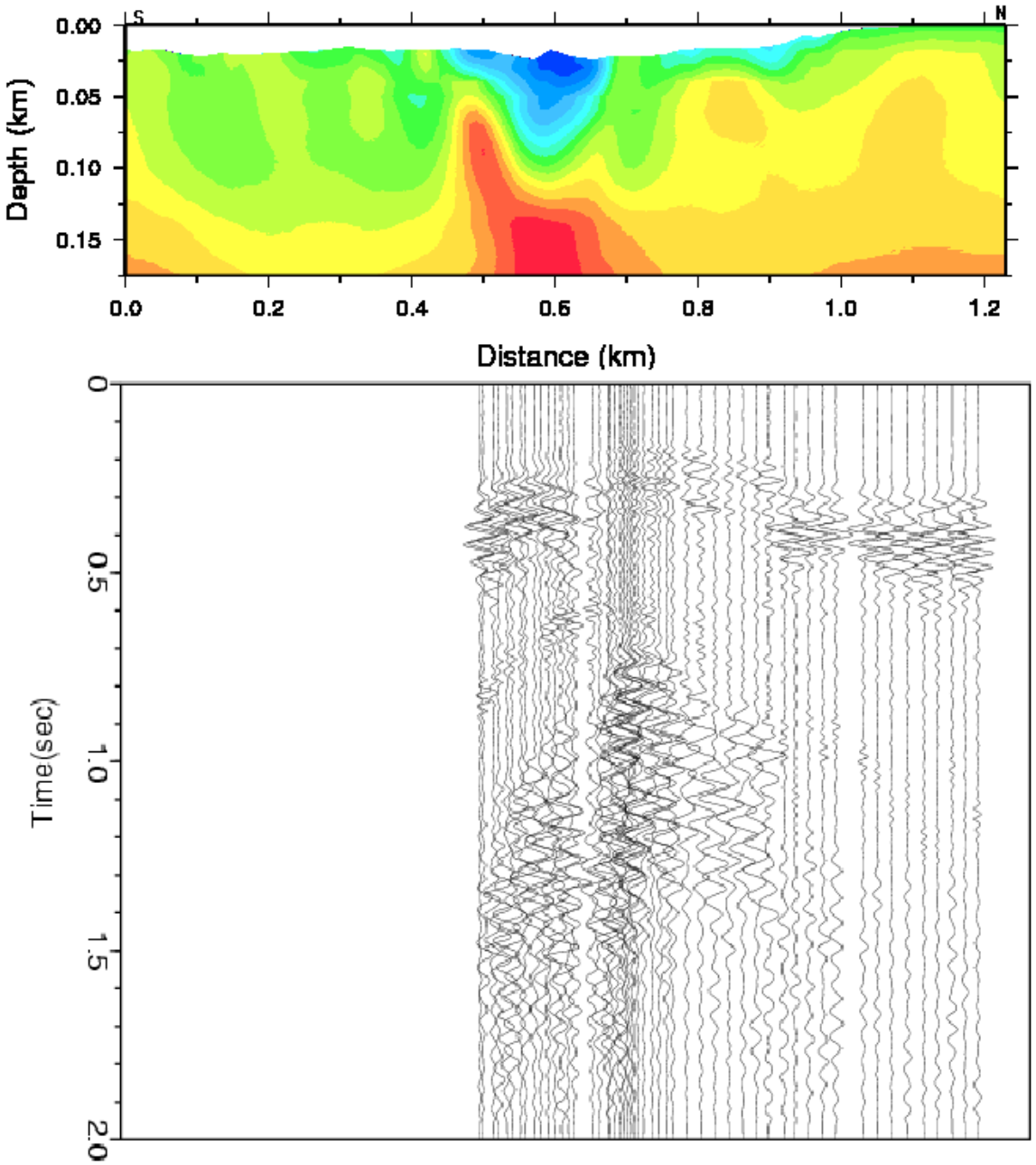

Figure 10. The final tomographic image and fan shot at a distance of 200 m.

The tomographic image along the 1.2 km profile shows significant heterogeneities with velocities varying from 0.7km/s to 2.2km/s. The fault was clearly exposed on the surface and the thickness of the sediments in the basin reaches up to several hundred meters. The northern part of İzmit Gulf essentially consists of young shallow sediments, beneath these lie a Triassic and Paleozoic sandstone, clay stone, and marn where relatively high velocities take place. P-wave velocities vary from 1.7–2.0 km/s down to 175 m depth. The velocities of the sediments, on the southern part corresponds to an olistolitic complex, which is composed of Eosen volcanics (schist, serpentinite, and andesite) (Doğan, B., 1998), differing from 1.4 to 1.7 km/s and decreases to 1.4 km/s within the fault zone down to 100–150 m depth.

Another low-velocity zone of 0.9km/s is observed adjacent to the 1999 İzmit earthquake fault zone and interpreted as an effect of the irrigation channel when the

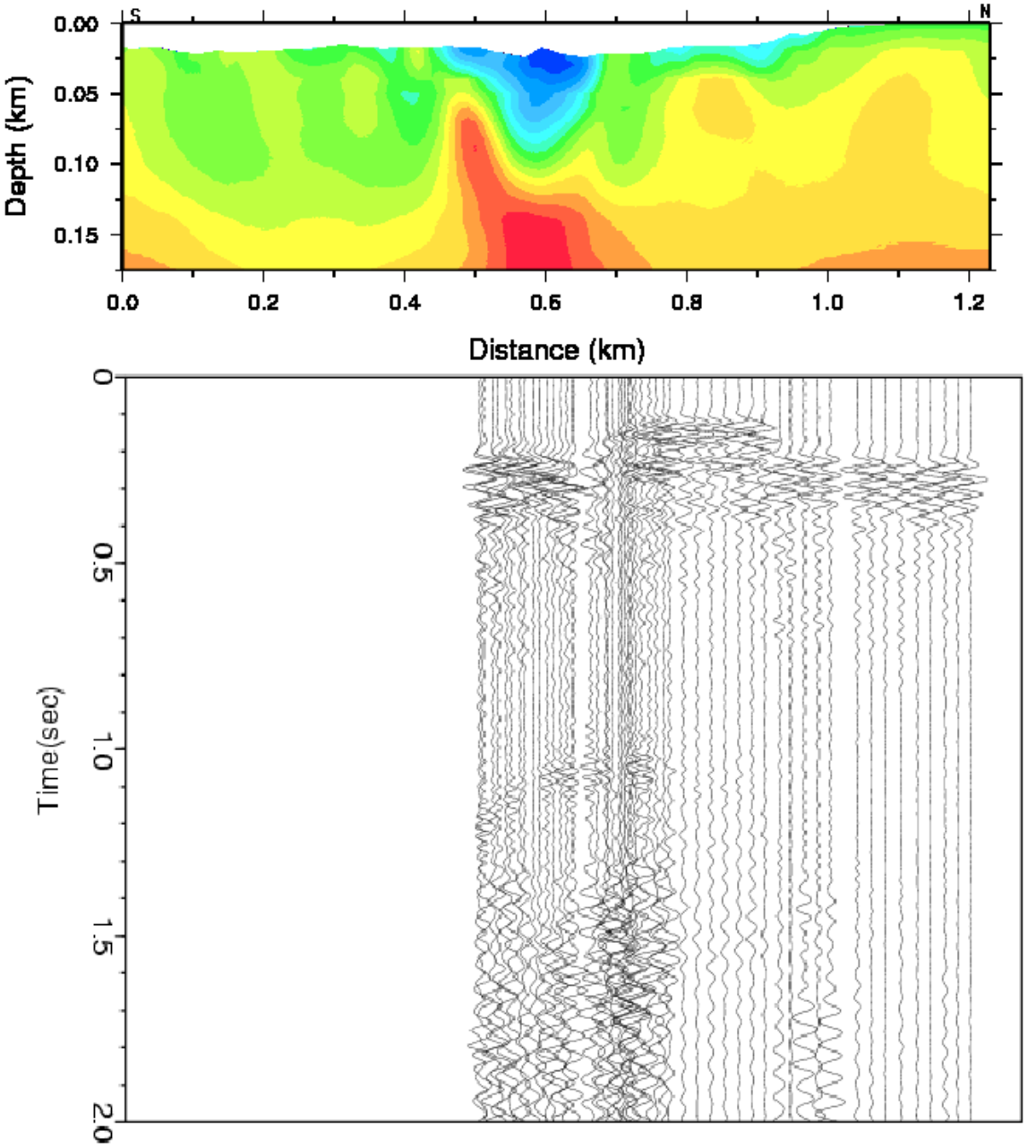

Figure 11. The final tomographic image and fan shot at a distance of 400 m.

geometry of the experiment is considered. A localized body of high velocity (2.2 km/s) with respect to the surrounding units, between 500–700 m is considered to be related to a buried andesitic ridge. However, since the recovered velocity model from the tomographic image is limited in depth, any conclusive interpretation on the distribution of this high velocity body is impracticable. After analyzing the fan shots, a significant asymmetry of the wavefield on both sides of the fault zone is realized. There is a large travel time jump between distances of 800 and 900 m. Such a travel time jump cannot be correlated with the final tomographic image. If the high-velocity anomaly is not local but has larger spatial dimensions or has continuity along the fault zone, it may create asymmetries on the wavefield together with travel time anomalies on the first arrivals as well as diffraction patterns on the wavefield. The clear diffraction patterns that are observed in the shot gathers, are an independent confirmation of the high-velocity anomaly observed on the tomographic image.

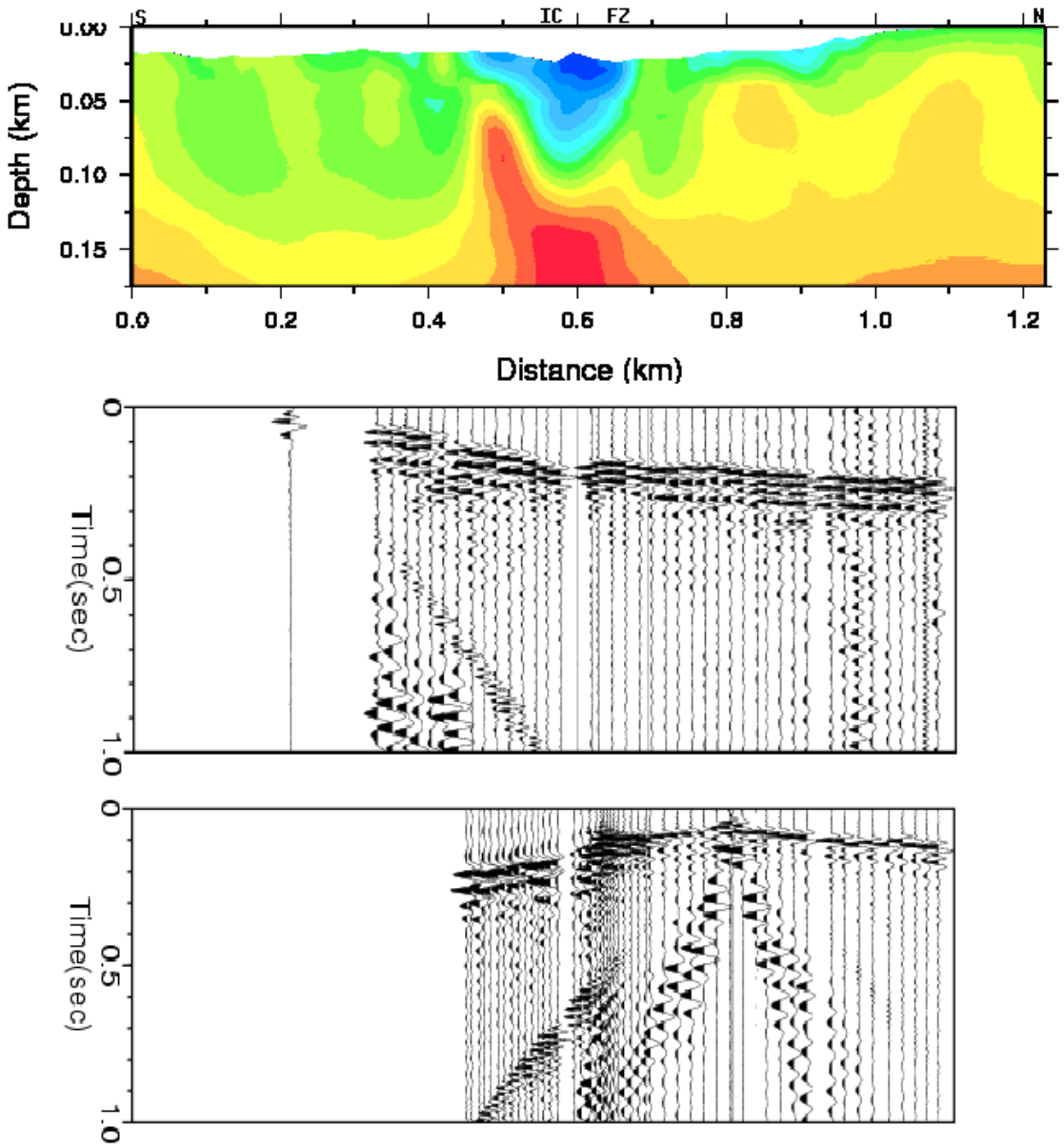

Figure 12. The final tomographic image and two shot gathers, which are plotted with a reducing velocity of 2 km/s, along the profiles.

The tomographic results clearly indicate that the fault zone is approximately 100 m wide and correlates well with previous studies such as the investigation of basin structures in the İzmit Bay area by single-station microtremor and gravimetric methods (Özalabey et al., 2011) and Shear wave velocity structure estimated from active–passive array surface wave and single-station microtremor methods (Zor et al., 2010).

Acknowledgements

I would like to express my special thanks to Prof. Dr. Hayrullah Karabulut for his precious contributions and valuable guidance. I also thank to Prof. Dr. Serdar Özalaybey for his precious comments. The seismic experiment would not be performed without the contributions of LGIT and TÜBİTAK-Marmara Research Center, Earth and Marine Sciences Research Institute. Some of the figures in this paper were produced using public domain software 'Generic Mapping Tools (GMT)' (Wessel & Smith 1998).

References

Aksoy ME (2002). İzmit–Sapanca arasının genç tektonik ve paleosismolojik özellikleri. Yüksek Lisans Tezi, İTÜ, Avrasya Yer Bilimleri Enstitüsü (in Turkish).

Aktar M, Özalaybey S, Ergin M, Karabulut H, Bouin MP et al. (2004). Spatial variation of aftershock activity across the rupture zone of the 17 August 1999 Izmit earthquake, Turkey. Tectonophysics 391: 325-334. https://doi.org/10.1016/j.tecto.2004.07.020

Barka A, Kadinsky-Cade K (1988). Strike-slip fault geometry in Turkey and its influence on earthquake activity. Tectonics 7: 663– 684. https://doi.org/10.1029/TC007i003p00663

Barka AA (1992). The North Anatolian fault zone. Annales Tectonicae 6: 164–195.

Barka AA, Akyüz HS, Altunel E, Sunal G, Çakir Z et al. (2002). The Surface rupture and slip distribution of the 17 August 1999 İzmit earthquake (M 7.4), North Anatolian Fault. Bulletin of the Seismological Society of America 92: 43–60. https://doi.org/10.1785/0120000841

Ben-Zion Y, Aki K (1990). Seismic radiation from an SH line source in a laterally heterogeneous planar fault zone. Bulletin of the Seismological Society of America 80 (4): 971-994. https://doi.org/10.1785/BSSA0800040971

Ben-Zion Y (1998). Properties of seismic fault zone waves and their utility for imaging low velocity structures. Journal of Geophysical Research 103 (B6): 12,567-12,585.

Ben-Zion Y, Peng Z, Okaya D, Seeber L, Armbruster JG et al. (2003). A shallow fault zone structure illuminated by trapped waves in the Karadere-Düzce branch of the north Anatolian fault, western Turkey. Geophysical Journal International 152: 699-717. https://doi.org/10.1046/j.1365-246X.2003.01870.x

Cormier VF, Spudich P (1984). Amplification of ground motion and waveform complexities in fault zones: examples from the San Andreas and the Calaveras faults. Geophysical Journal of the Royal Astronomical Society 79: 135-152. https://doi.org/10.1111/j.1365-246X.1984.tb02846.x

Doğan B, (1998). Yuvacık (İzmit)–Sapanca (Adapazarı) arası bölgenin jeolojisi ve tektonik özelllikleri. Yüksek Lisans Tezi. http://acıkbili.yok.gov.tr/handle/20.500121812/421862

Emre Ö, Duman TY, Özalp S, Elmacı H, Olgun Ş et al. (2013). Active Fault Map of Turkey with and Explanatory Text. General Directorate of Mineral Research and Exploration, Special Publication Series-30. Ankara-Turkey.

Fohrmann M, Jahnke G, Igel H, Ben-Zion Y (2001). Guided waves generated by sources outside a low velocity fault zone layer. Eos Transactions American Geophysical Union 82: F886.

Fohrmann M, Igel H, Jahnke G (2004). Guided Waves from Sources Outside Faults: An Indication for Shallow Fault Zone Structure. Pure and Applied Geophysics 161: 2125–2137. https://doi.org/10.1007/s00024-004-2553-y

Hole JA, Zelt BC (1995). Three-dimensional finite-difference reflection traveltimes. Geophysical Journal International 121: 427-434. https://doi.org/10.1111/j.1365-246X.1995.tb05723.x

Humphreys E, Clayton RW (1988). Adaptation of back projection tomography to seismic travel time problems. Journal of Geophysical Research 93: 1073-1085. https://doi.org/10.1029/JB093iB02p01073

Igel H, Ben-Zion Y, Leary PC (1997). Simulation of SH- and P-SV wave propagation in fault zones. Geophysical Journal International 12 8(3) : 533-546. https://doi.org/10.1111/j.1365-246X.1997.tb05316.x

Igel H, Jahnke G, Ben-Zion Y (2002). Numerical Simulation of Fault Zone Guided Waves: Accuracy and 3-D Effects. Pure and Applied Geophysics 9: 2067-2083. https://doi.org/10.1007/s00024-002-8724-9

Jahnke G, Igel H, Ben-Zion Y (2002). Three-dimensional calculations of fault zone guided waves in various irregular structures. Geophysical Journal International 151 (2): 416-426. https://doi.org/10.1046/j.1365-246X.2002.01784.x

Karabulut H, Bouin M, Bouchon M, Dietrich M, Cornou C et al. (2002). The seismicity in the Eastern Marmara Sea after the 17 August 1999 Izmit Earthquake. Bulletin of the Seismological Society of America 92: 382-393. https://doi.org/10.1785/0120000820

Karabulut H, Özalaybey S, Taymaz T, Aktar M, Selvi O et al. (2003). A tomographic image of the shallow crustal structure in the Eastern Marmara. Geophysical Research Letters 30: 2277-2280. https://doi.org/10.1029/2003GL018074

Leary PC, Li YG, Aki K (1987). Observation and modelling of fault zone fracture seismic anisotropy-I. *P, SV.* and *SH* traveltimes. Geophysical Journal of the Royal Astronomical Society 91: 461–484. https://doi.org/10.1111/j.1365-246X.1987.tb05239.x

Li YG, Vidale JE, Aki K, Xu F (2000). Depth-dependent structure of the landers fault zone from trapped waves generated by aftershocks. Journal of Geophysical Research 105: 6237-6254. https://doi.org/10.1029/1999JB900449

Malin PE (2020). Fault Zone Guided Waves. In: Gupta H. (eds) Encyclopedia of Solid Earth Geophysics. Encyclopedia of Earth Sciences Series. Springer, Cham. https://doi.org/10.1007/978-3-030-10475-7_269-1

McGuire J, Ben-Zion Y (2005). High-resolution imaging of the Bear Valley section of the San Andreas fault at seismogenic depths with fault zone head waves and relocated seismicity. Geophysical Journal International 162: 1-12. https://doi.org/10.1111/j.1365-246X.2005.02703.x

McKenzie D (1972). Active tectonics of the Mediterranean region. Geophysical Journal of the Royal Astronomical Society 30 (2): 109–185. https://doi.org/10.1111/j.1365-246X.1972.tb02351.x

Özalaybey S, Ergin M, Aktar M, Tapırdamaz C, Biçmen F et al. (2002). The 1999 İzmit Earthquake Sequence in Turkey: Seismological and Tectonic Aspects. Bulletin of the Seismological Society of America 92: 376-386. https://doi.org/10.1785/0120000838

Özalaybey S, Zor E, Ergintav S, Tapırdamaz MC (2011). Investigation of 3-D basin structures in the İzmit Bay area (Turkey) by single-station microtremor and gravimetric methods, Geophysical Journal International 186 (2) : 883-894. https://doi.org/10.1111/j.1365-246X.2011.05085.x

Peng Z, Ben-Zion Y, Michael AJ, Zhu L (2003). Quantitative analysis of seismic trapped waves in the rupture zone of the 1992 Landers, California earthquake: Evidence for a shallow trapping structure. Geophysical Journal International 155: 1021-1041. https://doi.org/10.1111/j.1365-246X.2003.02109.x

Peng Z, Ben-Zion Y (2004). Systematic analysis of crustal anisotropy along the Karadere-D¨uzce branch of the North Anatolian fault. Geophysical Journal International 159: 253-274. https://doi.org/10.1111/j.1365-246X.2004.02379.x

Peng Z, Ben-Zion Y (2006). Temporal changes of shallow seismic velocity around the Karadere-Düzce branch of the north Anatolian fault and strong ground motion. Pure and Applied Geophysics 163: 567-600. https://doi.org/10.1007/s00024-005-0034-6

Rovelli A, Caserta A, Marra F, Ruggiero V (2002). Can seismic waves be trapped inside an inactive fault zone? The case study of Nocera Umbra, central Italy. Bulletin of the Seismological Society of America 92: 2217-2232. https://doi.org/10.1785/0120010288

Şengör A (1979). Mid-Mesozoic closure of Permo–Triassic Tethys and its implications. Nature 279: 590–593. https://doi.org/10.1038/279590a0

Şengör AMC, Tüysüz O, İmren C, Sakınç M, Eyidoğan H et al. (2005). The north Anatolian fault: a new look, Annual Review of Earth and Planetary Sciences 33: 37-112. https://doi.org/10.1146/annurev.earth.32.101802.120415

Wessel P and Smith WHF (1998). New, improved version of Generic Mapping Tools released. *Eos, Transactions of the American Geophysical Union* 79 (47): 579. https://doi:10.1029/98EO00426

Vidale JE (1988). Finite-difference calculation of travel times. Bulletin of the Seismological Society of America 78: 2062-2076.

Yiğitbaş E, Elmas A, Sefunç A, Özer N (2004). Major neotectonic features of the North Anatolian Fault Zone: The development of the Adapazarı – Karasu corridor and its significance. Geological Journal 39: 179-198. https://doi.org/10.1002/gj.962

Zor E, Özalaybey S, Karaaslan A, Tapırdamaz MC, Tarancıoğlu ÇA et al. (2010). Shear wave velocity structure of the İzmit Bay area (Turkey) estimated from active-passive array surface wave and single-station microtremor methods. Geophysical Journal International 182 (3): 1603-1618. https://doi.org/10.1111/j.1365-246X.2010.04710.x